Article:
Rowsell, Benjamin, O'Brien, Harry, Athavan, Gayathri et al. (2024) The iron-catalysed Suzuki coupling of aryl chlorides. Nature Catalysis. pp. 1186-1198. ISSN: 2520-1158

https://doi.org/10.1038/s41929-024-01234-0

nature catalysis

Article

https://doi.org/10.1038/s41929-024-01234-0

The iron-catalysed Suzuki coupling of aryl chlorides

Received: 12 December 2022

Accepted: 12 September 2024

Published online: 17 October 2024

Check for updates

Benjamin J. S. Rowsell[1], Harry M. O'Brien[1], Gayathri Athavan[1], Patrick R. Daley-Dee[1], Johannes Krieger[2], Emma Richards[3], Karl Heaton[4], Ian J. S. Fairlamb[4] & Robin B. Bedford[1]

The very widely exploited Suzuki biaryl coupling reaction typically requires catalysts based on palladium, but there is an increasing desire to replace this metal with a more sustainable, less expensive alternative, with catalysts based on iron being a particularly attractive target. Here we show that a simple iron-based catalyst with an N-heterocyclic carbene ligand can be used to excellent effect in the Suzuki biaryl coupling of aryl chloride substrates with aryl boronic esters activated by an organolithium reagent. Mechanistic studies suggest the possible involvement of Fe(I) as the lowest oxidation state on the catalytic manifold and show that the challenging step is not activation of the aryl chloride substrate, but rather the transmetallation step. These findings are likely to lead to a renaissance of iron-catalysed carbon–carbon bond-forming transformations with soft nucleophilic coupling partners.

The Suzuki cross-coupling reaction[1–4] (Fig. 1) represents a powerful method for the synthesis of compounds containing a biaryl motif and as such is widely exploited in commercial applications. These include the synthesis of *o*-tolyl benzonitrile (OTBN)—an intermediate for the production of a number of sartan hypertension drugs, for example valsartan—and Boscalid—a broad-spectrum fungicide used in crop protection[5]. The overwhelming majority of Suzuki biaryl coupling reactions employ palladium-based catalysts; however concerns exist regarding the cost, sustainability and toxicity of this metal in coupling reactions, and therefore a drive exists to replace palladium catalysis with more sustainable approaches[6,7].

The most extensive advances in this regard have so far been with nickel-based[8–13] and copper-based[14–17] catalysts, although cobalt is proving increasingly useful[18–23]. Iron represents the ideal first-row transition metal for replacing palladium in Suzuki biaryl cross-coupling reactions as it is very cheap, widely available and relatively non-toxic. While the iron-catalysed Suzuki coupling of alkyl-based electrophiles has been reasonably widely investigated[24–32], the equivalent biaryl cross-coupling remains elusive, although a reaction performed at 15,000 bar has been described[33]. Indeed, aside from claims that we have subsequently shown to be unfounded[21,34], currently reported iron-catalysed Suzuki biaryl cross-couplings under synthetically reasonable conditions require either an activated heteroaryl substrate[24] or the use of substrate-directed C–X activation[35,36].

Herein we demonstrate that the elusive iron-catalysed Suzuki biaryl cross-coupling of simple aryl chloride substrates with aryl boronic esters is indeed achievable. Mechanistic investigations suggest the lowest oxidation state on the iron in the manifold is likely Fe(I) and that oxidative addition of the aryl chlorides to Fe(I) is facile. By contrast, transmetallation appears to be the challenging step in the potential manifolds investigated.

Results

Optimization studies

In the first instance we investigated the coupling of chlorobenzene (**1a**) with **2a**, the aryl boronate formed by reaction of the corresponding parent aryl boronic ester with ^{t}BuLi (^{t}Bu, *tert*-butyl). We previously found that some N-heterocyclic carbene (NHC) ligands worked well in iron-catalysed substrate-directed Suzuki biaryl coupling[36] so we screened their performance with $FeBr_3$ as the iron source (selected data, Fig. 2b; full data, Supplementary Tables 2 and 3). In most cases, 10% or less of the desired cross-coupled product **3a** was obtained; however, when 1,3-dimesitylimidazol-2-ylidene (IMes) was exploited, a modest 24% of **3a** resulted, albeit accompanied by a considerable amount of

[1]School of Chemistry, University of Bristol, Bristol, UK. [2]Merck Healthcare KGaA, Darmstadt, Germany. [3]Cardiff Catalysis Institute, Cardiff University, Cardiff, UK. [4]Department of Chemistry, University of York, York, UK. e-mail: r.bedford@bristol.ac.uk

https://doi.org/10.1038/s41929-024-01234-0

homo-coupled by-product **4a**. Replacing $FeBr_3$ with other iron sources gave a poorer performance (Supplementary Table 5), while a very poor performance was obtained with phosphine ligands in place of IMes (Supplementary Table 4). A solvent screen (Supplementary Table 7) revealed a 1:1 mixture of 1,4-dioxane/2-methyl tetrahydrofuran to be optimal out of the solvent systems tested, in part due to the higher reaction temperature (100 °C) this mixture allowed. An appropriate halide additive is essential for activity, with $MgBr_2$ faring best out of those tested (Supplementary Table 9).

Reaction profiles obtained during the catalytic studies (for example, Fig. 5c below) showed the presence of an induction period of around 30–45 s; we reasoned this may be due to either deprotonation of the NHC precursor or a reduction of the resultant iron pre-catalyst. Accordingly, we investigated the effect of adding a catalytic quantity of activators that might accelerate one or both of these processes (Supplementary Table 8) and found that MeMgBr (1 equiv. per Fe) worked best. Mechanistic studies (below) suggest that the role of the Grignard reagent is to deprotonate the ligand precursor, rather than to reduce the iron pre-catalyst. Other additives such as NMP (*N*-methylpyrrolidone), TMEDA (1,2-(dimethylamino) ethane) and PEG (polyethylene glycol) that were previously found to give increased performance in iron-catalysed cross-coupling reactions[37–44] proved to be ineffective here (Supplementary Tables 10 and 11). Finally, the loading of **2a** was adjusted (Supplementary Table 12), which furnished the optimized conditions outlined in Fig. 2c.

Substrate scope

With the optimized conditions in hand, we next turned our attention to examining the scope and limitations of the transformation. In all cases, we obtained varying amounts of by-products **4**, furnished by competitive homo-coupling of the nucleophilic coupling partners **2**, but in almost all cases this could be readily removed from the desired cross-coupled products **3** by column chromatography. Figure 3 summarizes the successful coupling of a range of aryl chlorides **1** and aryl boronates **2**. Unsuccessful coupling reactions are detailed in the Supplementary Methods (Supplementary Figs. 1 and 2), as are coupling reactions with other aryl halides and pseudohalides, which tended to give little of the desired products (Supplementary Table 1).

Both electron-withdrawing and electron-donating groups in the para position of the aryl chloride were well tolerated and typically gave higher yields of the desired products (**3b**–**3j**) than the unsubstituted variant (**3a**). From this information alone, it is not possible to draw any clear mechanistic conclusion, but this will be returned to in the mechanistic sections below, where data for linear free energy relationships are presented. Similarly, no clear conclusions can be drawn about the effect of *meta* substitution on performance. The introduction of steric bulk into the *ortho* position does not unduly impact activity (**3r**, **3t** and **3u**), however the 2,6-dimethyl phenyl substituent leads to reduced yield of the cross-coupled product **3v**. Amide and ester functions were tolerated on the aryl chloride substrates, but ketonic or aldehydic groups were not (Supplementary Fig. 1). Aryl chlorides with secondary or tertiary amino groups coupled well (products **3i**, **3j** and **3q**), but a primary aniline did not give the desired product (Supplementary Fig. 1); likewise unprotected phenol-based and thiophenol-based substrates were not tolerated.

Varying the *para* substituent of the activated aryl boronic ester again gave no readily identifiable electronic trend for the reaction; but this subject will be returned to in an analysis of the linear free energy (below). A range of heteroaryl chlorides also couple well under the optimized conditions, and the results from this study are summarized in Fig. 4. By contrast, heterocyclic functionality on the nucleophilic coupling partner was not tolerated, with none of the desired products obtained with boron esters based on 3-pyridyl, 4-pyridyl, 2-thiophenyl, 7-quinolinyl or 2-benzofuryl substrates (Supplementary Fig. 2).

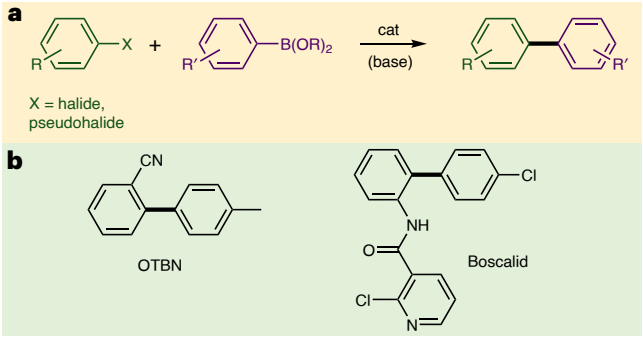

Fig. 1 | The Suzuki biaryl coupling reaction. a, The general catalytic coupling process. cat, catalyst. **b**, Selected commercial applications with the bond formed by Suzuki coupling highlighted.

Confirming the active role of iron

Iron is essential for the reaction, with only trace activity observed when $FeBr_3$ was omitted from the reaction mixture (Supplementary Section 5.1 and Supplementary Table 13). Typically, 98.5% purity $FeBr_3$ was employed for the majority of the studies, with material sourced from three different suppliers. $FeBr_2$ (98%+) gave a slightly reduced yield (53% of **3a**) compared with the tribromide, but its use allowed a comparison of the kinetic profiles obtained with 98% and 99.995% $FeBr_2$, which gave essentially indistinguishable performances (Supplementary Table 13 and Supplementary Fig. 3), indicating that trace impurities in the iron precursor are unlikely to be responsible for the observed activity. Similar results were also obtained when samples of $FeCl_3$ of 98% and 99.99% purity were used under the reaction conditions (Supplementary Fig. 3). The undetected presence of substantial amounts of palladium in Suzuki cross-coupling has led to misplaced claims[45] that were subsequently corrected[46–48]. Accordingly, addressing the levels of palladium impurities was specifically targeted by using inductively coupled plasma mass spectrometry (ICP-MS), employing a robust digestion protocol (Supplementary Methods for details). The level of palladium impurities in dried samples of reaction mixtures catalysed by the 98% and 99.995% purity $FeBr_2$ were found to be relatively high at between 1 and 2 ppm (Supplementary Methods for data). Examination of the palladium in samples of 98.5% purity $FeBr_3$ and 98% and 99.995% purity $FeBr_2$ showed they contain levels well below these values; triplicate studies on 100 mg samples gave ranges of 230–390 ppb, 23–200 ppb and 76–281 ppb, respectively. Therefore, the iron salts contribute only minor amounts (~1% or less) to the total palladium impurities; indeed ICP-MS analysis of a reaction mixture without added iron bromide showed a palladium loading of 3 ppm, confirming that the main source of palladium is one or more of the other reaction components. Of critical importance, the almost complete absence of catalytic activity in the absence of the iron salts shows that the palladium impurities present are not responsible for the observed catalysis in the presence of iron. An important side note to researchers examining potential impurities by ICP-MS is the observation of the wide variability of the ICP-MS data for the same sample of iron salts; it seems that the palladium impurities can be somewhat heterogeneously distributed throughout the sample, and therefore testing multiple samples is important, as is the amount of the sample used, with a noticeable increase in variability observed on reducing sample size from 100 mg to 10 mg (Supplementary Methods and Supplementary Table 14 for details).

Determining the lowest oxidation state of the catalyst

Moving on to the iron catalysis, a key question with any cross-coupling reaction is what the lowest relevant oxidation state obtained in the catalytic manifold is[49]. The lowest possible oxidation state accessed by the metal in the presence of the reducing (nucleophilic) coupling

https://doi.org/10.1038/s41929-024-01234-0

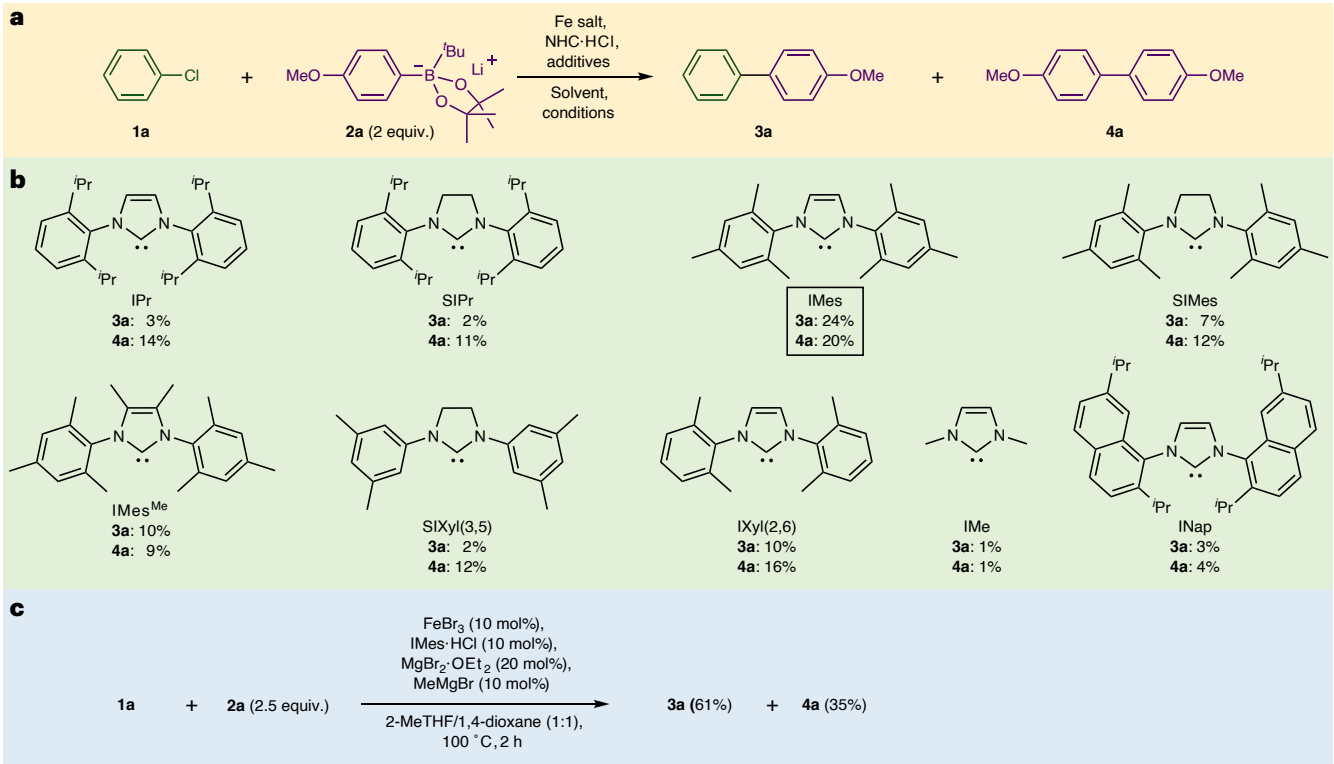

Fig. 2 | Selected optimization data. a, The model reaction employed for the majority of the optimization studies. **b**, Effect of varying the five-membered NHC ligands (introduced as the corresponding HCl salts). **c**, The optimized reaction conditions. Yields of **3a** and **4a** based on **1a** and **2a**, respectively, determined by GC (dodecane internal standard). Full optimization study results given in Supplementary Methods. Pr, propyl; ^{i}Pr, isopropyl; IPr, 1,3-bis(2,6-diisopropylphenyl)imidazolidin-2-ylidene; SIPr, 1,3-bis(2,6-diisopropylphenyl)-4,5-dihydro-2H-imidazol-2-ylidene; SIMes, 1,3-bis(mesityl)-4,5-dihydro-2H-imidazolidin-2-ylidene; IMes^{Me}, 1,3-bis(mesityl)-4,5-dimethylimidazolidin-2-ylidene; SIXyl, 1,3-bis(3,5-di-methylphenyl) imidazolidin-2-ylidene; IXyl, 1,3-bis(3,5-di-methylphenyl)-4,5-dihydro-2H-imidazolidin-2-ylidene; IMe, 1,3-dimethylimidazolidin-2-ylidene; INap, 1,3-bis(2,7-diisopropylnaphthyl)imidazolidin-2-ylidene.

partner places an absolute limit on the thermodynamically accessible low oxidation state; however, this low oxidation state may not be kinetically relevant to catalysis if the full reduction is too slow.

We have previously shown that $FeCl_2$/IMes can be reduced to Fe(0) by the organoboronate Li[Ph(^{t}Bu)Bpin], **2b** (pin, pinacolato; ref. 36), and in the presence of dvtms (1,3-divinyltetramethyldisiloxane), the iron(0) complex, **5** (ref. 50), is formed (Fig. 5a). We find here that complex **5** is also produced by the reduction of $FeBr_3$ in the presence of IMes and dvtms using **2a** as the reductant (Fig. 5a; Supplementary Methods for details). The use of IMes·HCl in place of IMes gave the same result showing that the boronate **2a** is sufficiently basic to deprotonate the NHC under catalytic conditions. Adding MeMgBr (Me, methyl) to the reaction mixture led to the formation of **5**, but when the boronate **2a** was omitted, the Fe(0) complex was not observed, suggesting that contrary to our initial hypothesis, the MeMgBr may not facilitate pre-catalyst reduction but may simply act as an additional base to aid deprotonation of the NHC precursor. The presence or absence of $MgBr_2$ does not appear to have an impact on whether or not **5** is formed. The Fe(0) complex **5** is a competent pre-catalyst, although it gave a slight reduction in the yield of **3a** (57%). As is true with all transition metal-based homogeneous catalysis, the oxidation state of the pre-catalyst gives no information as to the oxidation states of the active species on the catalytic manifold.

Clearly the boronate **2a** is able to reduce the Fe(III) precursor all the way to Fe(0), indicating that it is a thermodynamically accessible oxidation state available under the catalytic reaction conditions. However, this result does not necessarily mean that Fe(0) species are kinetically relevant during catalysis. The plots of formation of **3a** against time with varying pre-catalyst concentrations make clear that an induction period exists in the formation of cross-coupled product (Fig. 5c), while no such delay is seen in the formation of **4a** (Fig. 5d), consistent with activation of the pre-catalyst being a reductive process, triggered by reaction with **2a**. Figure 5e shows an overlay of the formation of **3a** and **4a** in a standard reaction at 8.3 mM pre-catalyst concentration, with the formation of **4a** under the same conditions but with no chlorobenzene present. This result makes it apparent that essentially all of the homo-coupled **4a** observed during the first 1.25 min is due to the reduction of the pre-catalyst mixture. Looking at the maximum rate of formation of the cross-coupled product, this occurs from 1.25 min onward, after the bulk of the iron has been reduced to an average oxidation state of Fe(I). Previous work by Norrby and coworkers indicated a similar reduction to Fe(I) in the iron-catalysed Kumada coupling of aryl Grignard reagents in the absence of strongly coordinating co-ligands[51–53]. Similarly, we have shown that well-defined Fe(I) complexes with chelating bisphosphine ligands can form under catalytic conditions in the Negishi coupling of aryl zinc reagents[54], although it was subsequently shown that in this case the bisphosphines were not coordinated to the iron centre during catalysis[55]. The results obtained here suggest the lowest oxidation state on the catalytic manifold for cross-coupling may be Fe(I); however, this result must be treated with some caution: the lowest oxidation state may feasibly be Fe(II), and the lag in induction may be due to a secondary post-reduction process.

Figure 5f shows the results from a reaction in which the electrophile **1a** was added 1.75 min after the addition of the nucleophile **2a**. The iron is clearly reduced before the addition of the electrophile, and a plateau of homo-coupled product **4a** is produced that corresponds with the bulk oxidation state of the iron lying between Fe(I) and Fe(0) before the electrophile is added, at which point cross-coupling to

https://doi.org/10.1038/s41929-024-01234-0

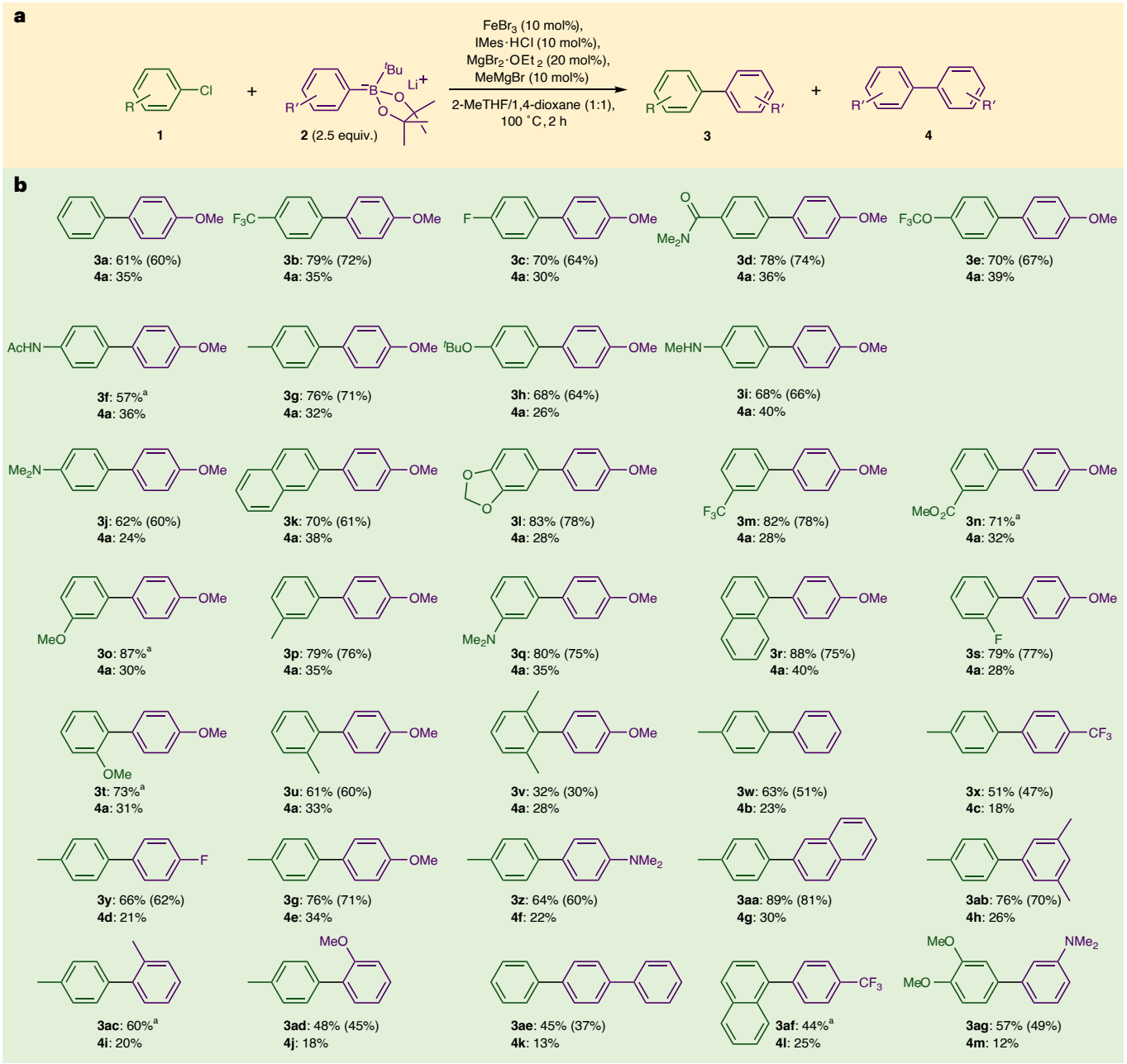

Fig. 3 | Selected substrate scope in the coupling of aryl chlorides. a, Reaction conditions. **b**, Variation of aryl chloride **1** and activated aryl boronate **2**. Ac, acetyl. Yields determined by NMR (1,3,5-trimethoxybenzene as internal standard); isolated yields shown in parentheses. [a]The results could not be separated from corresponding compound **4**.

produce **3a** starts without any further induction period, confirming that catalyst induction is reductive.

To explore catalyst speciation under kinetically relevant conditions, we undertook a series of investigations trying to trap Fe(0) or Fe(I) formed during the induction period. A mixture of $FeBr_3$, IMes and $MgBr_2{\cdot}OEt_2$ (Et, ethyl) was reacted with an excess of **2a** in the presence of dvtms, to monitor the formation of Fe(0) under these conditions. As described above, dvtms acts as a competent trapping agent, coordinating to any Fe(0) generated to produce the well-defined complex **5**, a process that could be monitored by ^{1}H NMR spectroscopy. A reaction aliquot collected after 5 min of heating showed approximately 7% conversion of the iron species to complex **5** as determined by ^{1}H NMR spectroscopy (Supplementary Methods for details). However much of this could be attributed to a slow background formation of **5** at room temperature prior to sample acquisition. To exclude the interference of room-temperature reactivity, an aliquot of the reaction mixture was isolated after 1 min of heating and stored at −78 °C prior to spectrum acquisition. This showed no measurable formation of complex **5**, indicating that reduction by the boronate to Fe(0) can be disregarded. However, this is not the only possible route to Fe(0) in the manifold; for instance disproportionation of Fe(I) to Fe(0) and Fe(II) might occur. We return to this subject below in the section 'Computational investigation of tentative catalytic cycles'.

Attempts at identifying intermediates were also made by employing liquid injection field desorption/ionization mass spectrometry (LIFDI-MS) and electron paramagnetic resonance (EPR) spectroscopic studies (Supplementary Methods for full details). The LIFDI-MS spectrum of a reaction aliquot collected at 10 min from the catalytic reaction, in the absence of chlorobenzene, showed a peak at a mass to charge ratio m/z = 741.50691, possibly consistent with the mass for

https://doi.org/10.1038/s41929-024-01234-0

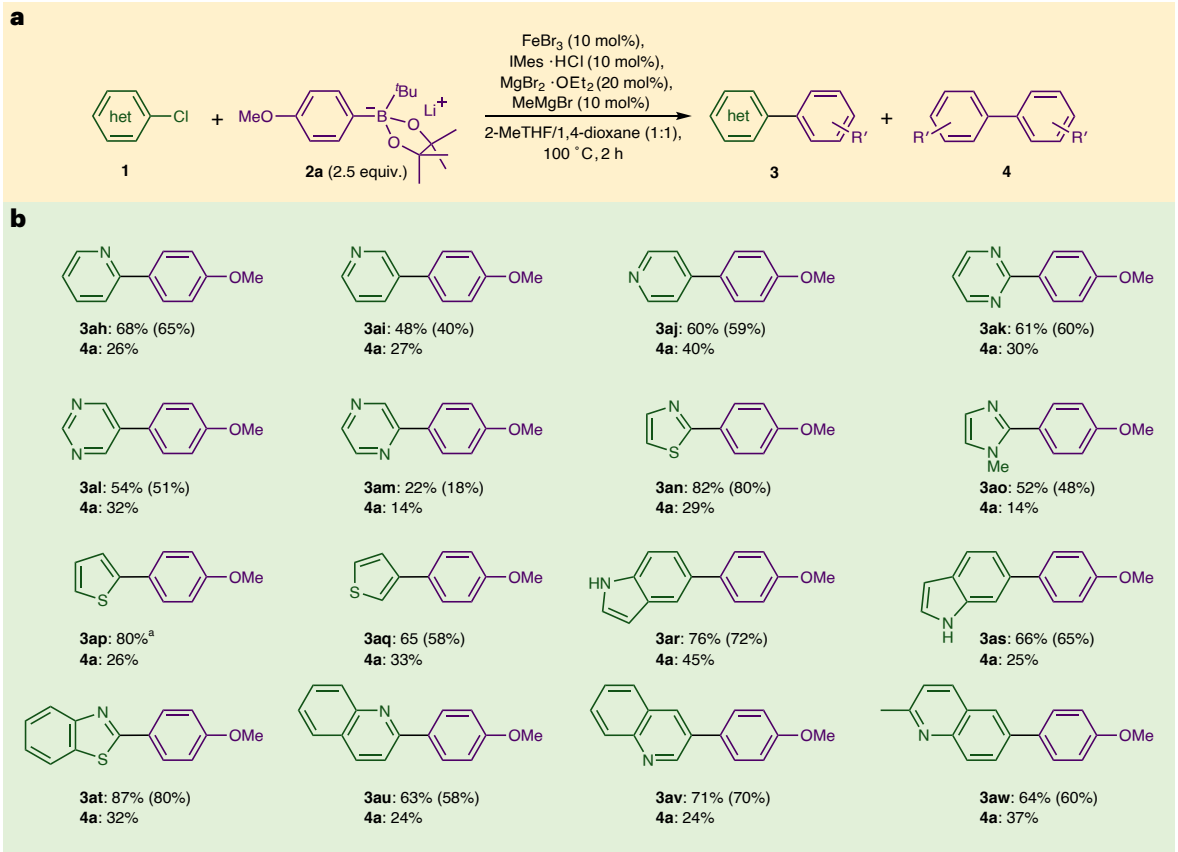

Fig. 4 | Selected substrate scope in the coupling of heteroaryl chlorides. a, Reaction conditions. **b**, Variation of heteroaryl chloride **1**. het, heteroaromatic. Yields determined by NMR (1,3,5-trimethoxybenzene as internal standard); isolated yields shown in parentheses. [a]The result could not be separated from corresponding compound **4**.

$[(IMes_2FeBr)\text{-}2H]^+$ (calculated $m/z = 741.2255$) but with an equivocal isotope distribution pattern due to low peak intensity (Supplementary Fig. 9). Note that catalytic reactions submitted for LIFDI-MS were performed in either 2-methyl tetrahydrofuran (2-MeTHF) or THF (the 1:1 mixture with 1,4-dioxane could not be used here due to freezing of the sample in the LIFDI emitter in the MS source; see Supplementary Methods for full details). An X-band EPR spectrum of a sample of a catalytic reaction without the aryl chloride substrate, removed at 1.5 min and recorded at 130 K, did not show evidence of any spin $S = 1/2$ species (Supplementary Fig. 10), but instead showed data consistent with an $S = 5/2$ system, which at this stage has not been analysed further. We reasoned that addition of a tridentate chelating trisphosphine (triphos) might lead to the trapping of a low-spin ($S = 1/2$) intermediate of the form [FeX(IMes)(triphos)] (X = aryl, halide) analogous to previously investigated Fe(I) species[28,54,56]. The spectra shown in Supplementary Fig. 10 show that at least two $S = 1/2$ species are formed: the major one of these, which forms more quickly, shows no hyperfine coupling to phosphorus, while the second grows in more slowly over time, suggesting it is not relevant to catalysis. A brief computational study on possible candidates for the low-spin Fe(I) intermediates (Supplementary Methods) did not help in the identification of the observed species. Therefore, while the observed formation of the major $S = 1/2$ species is consistent with the formation of a low-spin Fe(I) species, we do not currently know the exact nature of this complex (beyond it being phosphine free), and the fact that its formation appears to be triggered by the addition of the phosphine ligand may well preclude its involvement under genuine catalytic conditions.

Summarizing, reduction to Fe(0) by the boronate nucleophile **2a** does not appear to occur fast enough for it to be formed in appreciable amounts in the induction phase, but this does not, at this stage, rule out Fe(0) being formed in the manifold by disproportionation of Fe(I) (more below). Therefore, while compelling direct evidence of Fe(I) being the most reduced species formed in a timely manner during catalyst induction remains elusive, this seems most likely from the extent of homo-coupling of the nucleophile.

Rate investigations

The initial rates method proved challenging due to the observed induction periods; accordingly the 'initial rate' used in the analysis was the maximum rate observed immediately after the induction period. Notwithstanding the possible issues with this approach, the dependence of rate on catalyst concentration broadly appears to vary from approximately first-order dependence at lower catalyst loadings to what appears to be zero order at higher loadings (Supplementary Figs. 14 and 15 and Supplementary Table 16). To probe this further, we also adopted Burés's variable time-normalized analysis[57], which makes use of all the available data. Again, as seen with the initial rates approach, no single order gave an overlay of the data (Supplementary Fig. 16); however, the plots at the lowest catalyst loadings (5, 7.5 and 10 mol%) show a fractional order, with a good fit for the latter two obtained from a 0.5-order plot, while a zero-order fit is seen for the plots at 15 and 20 mol% (Supplementary Figs. 17–20 and Supplementary Table 16). Meanwhile the best overlay of the data for the formation of homo-coupled product **4a** in the reactions—as measured after the induction period in order to avoid issues with the formation of **4a** by an alternative process during pre-catalyst induction—occurs when the data are plotted assuming a first-order dependence at all but the lowest catalyst loadings (Supplementary Figs. 24–28 and Supplementary Table 16). Clearly, while the latter suggests a reasonably simple dependence of the rate of

https://doi.org/10.1038/s41929-024-01234-0

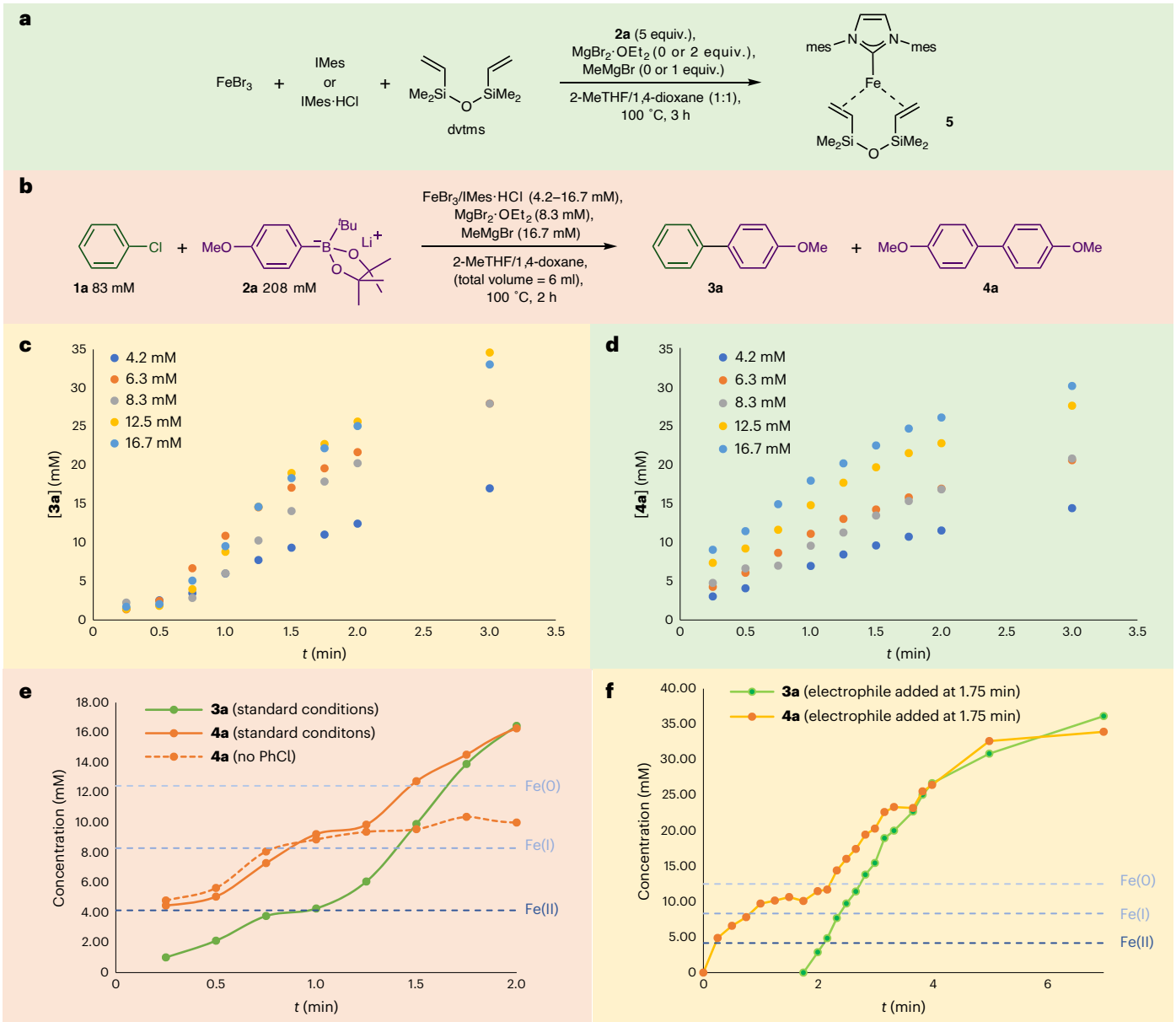

Fig. 5 | Mechanistic investigations on pre-catalyst activation. a, Reduction of $FeBr_3$/IMes and trapping of resultant Fe(0) with dvtms to give complex **5**. **b**, Reaction conditions employed for determining rates of formation of cross-coupled (**3a**) and homo-coupled (**4a**) products. **c**, Effect of varying catalyst concentration on rate of formation of **3a**. *t*, time. **d**, Effect of varying catalyst concentration on rate of formation of **4a**. **e**, Comparison of the formation of **3a** and **4a** in a standard reaction at 8.3 mM pre-catalyst concentration with the formation of **4a** under the same conditions but with no chlorobenzene. **f**, Formation of **3a** and **4a** in a reaction in which the electrophile **1a** was added 1.75 min after the addition of the nucleophile **2a**.

homo-coupling versus pre-catalyst concentration, the same is not true for the cross-coupling.

The initial rates method approach was used to determine the influence of the concentration of the reaction components on the rate of formation of both the cross-coupled product **3a** and the homo-coupled product **4a** in the coupling of chlorobenzene (**1a**) with the aryl boronate salt (**2a**). As described above, in all cases an induction period was observed; accordingly, the initial rates data used in the kinetic analyses were drawn from rates of conversion after the induction phase, and the data are summarized in Supplementary Figs. 29–36 and Supplementary Table 16. Fractional order dependencies of the initial rate on a chlorobenzene (**1a**) concentration of ~0.7 (saturating at the highest concentrations) and of ~0.3 were, respectively, observed for the heterocoupled (**3a**) and homo-coupled (**4a**) products. The rate of cross-coupling showed an approximately first-order (0.9) dependence on [**2a**], while the rate of homo-coupling of **2a** somewhat surprisingly showed a fractional order (0.4) dependence on [**2a**]. The fractional order dependencies of the cross-coupling and homo-coupling reactions are suggestive of complex, interlinked processes. Meanwhile the weak, but non-zero-order, dependence of the rate of homo-coupling of the boronate substrate on [PhCl] suggests that while PhCl is not incorporated into the homo-coupled product **4a**, the product's formation is influenced by [PhCl] (Ph, phenyl).

Considering the impact of additives, the rate of formation of cross-coupling product is essentially independent of the concentration of MeMgBr (Supplementary Figs. 37–40 and Supplementary Table 16). A fractional order (0.3) dependence of the concentration of added $MgBr_2$ on the rate of formation of the cross-coupled product **3a** is observed (Supplementary Fig. 42 and Supplementary Table 16) up to a loading of 25 mol%; beyond this point, further addition is

https://doi.org/10.1038/s41929-024-01234-0

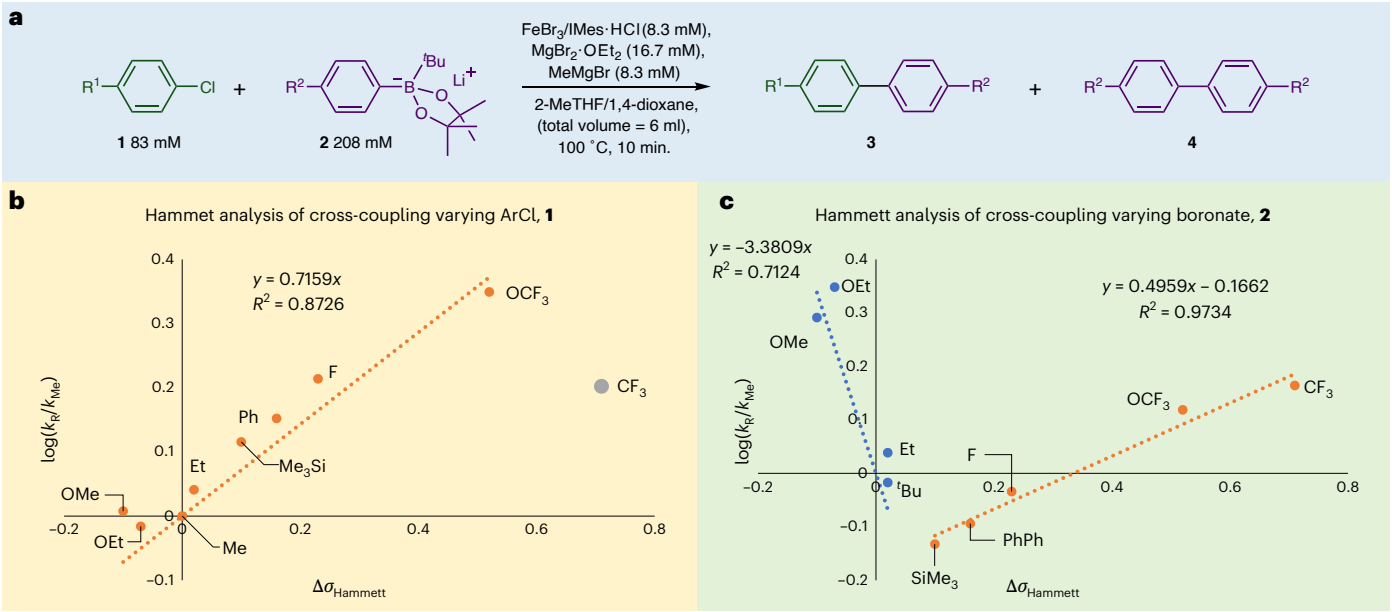

Fig. 6 | Linear free energy investigation. a, Reaction conditions. **b**, Effect of varying the substituents on the aryl chloride **1** on relative rates (aryl boronate, **2b**). **c**, Effect of varying substituents on the aryl boronates (aryl chloride, **1a**). Note $\log(\frac{k_R}{k_{Me}})$ rather than $\log(\frac{k_R}{k_H})$, where k_H is the rate with an unspecified substrate, was used throughout; $\Delta\sigma_{Hammett} = (\sigma_{Hammett}\ 4\text{-R}) - (\sigma_{Hammett}\ 4\text{-Me})$. k_{Me}, rate with methyl-subsituted substrate; k_R, rate with specified substrate.

deleterious. A similar variable dependence of the rate of formation of the homo-coupled product **4a** on [$MgBr_2$] is observed (Supplementary Fig. 44 and Supplementary Table 16).

Summarizing, the fractional and, in the case of the catalyst concentration, variable orders observed in the desired cross-coupling reaction indicate a complex manifold, possibly with competing pathways and/or varying nuclearity of catalytic iron intermediates.

Arrhenius plots for the cross-coupling of **1a** with **2a** and the competitive homo-coupling of **2a** (Supplementary Fig. 46) revealed activation energies of 82 and 84 kJ mol^{-1}, respectively, consistent with the substantial amounts of homo-coupling observed in the cross-coupling reactions. Meanwhile Eyring plots gave values for the Gibbs free energy of the transition state ($\Delta G^{\ddagger}$) at 298 K of **3a** and **4a** of 93 and 94 kJ mol^{-1}, respectively (Supplementary Fig. 47).

Linear free energy studies were also undertaken[58], using the reactions outlined in Fig. 6a, and the results for the cross-coupling reactions are summarized in Fig. 6b,c. Figure 6b reveals a positive Hammett dependence for the rate of formation of the cross-coupled products **3** on *para* substitution for all aryl chlorides except for the most electron-deficient example (*p*-chlorotrifluoromethyl benzene). The positive value of the reaction rate constant (ρ) of 0.7 is rather low compared with reactions that proceed via oxidative addition of aryl halides to nickel[59]. This suggests that either the build-up of negative charge on the *ipso* carbon during oxidative addition is substantially less pronounced on iron compared with nickel, or that the trend in relative rates is not a reflection of the C–Cl bond activation, but instead indicates the influence of an aryl ligand—derived from the aryl chloride—on an Fe centre at a later step in the catalytic cycle.

Figure 6c shows the variation in rates of cross-coupling against the Hammett values of the *p*-substituted aryl boronate salts **2**. This makes clear that a change in the mechanism exists, with the more electron-rich nucleophiles showing a negative ρ value (−3.4), while more electron-deficient substrates show a positive ρ (0.5). A similar behaviour is seen in the formation of the homo-coupled products **4** (Supplementary Fig. 57).

The influence of *para* substitution of the aryl chloride on the rate of homo-coupling of the nucleophile to give biphenyl (**4b**) proved less clear-cut. Plotting the log of relative rates against Hammett values gave a scatter ($r^2 = 0.29$, where r is the correlation coefficient; Supplementary Fig. 53); meanwhile, replacing the Hammett values with Creary values—a scale derived using a relatively apolar radical reaction[60]—gave an improved but still poor correlation ($r^2 = 0.45$; Supplementary Fig. 54). Norrby and coworkers found that incorporation of some Hammett character into the σ values (where σ is the Hammett σ constant) derived by Creary—in order to reflect some polar character in radical-based C–X bond cleavage—could substantially improve the correlation in iron-based oxidative addition[61]. This proved to be the case here, with values derived from a combination of Creary and Hammett parameters (3:1) giving a modest correlation ($r^2 = 0.74$; Supplementary Fig. 55).

The appearance of very different linear free energy dependencies on *para* substitution of the aryl halides in the formation of **3** and **4** implies quite different influences of the substitution pattern on these two transformations, with the latter showing some radical behaviour. Clearly, the aryl chloride plays a role in homo-coupling of the nucleophile, most likely by acting as an oxidant to counter the reductive coupling of the nucleophile. Indeed a mass balance study (Supplementary Methods) on the coupling of **2a** with 4-fluorochlorobenzene showed that the amount of **4a** produced by homo-coupling of the nucleophile corresponds approximately to the amount of 4,4′-difluorobiphenyl produced by homo-coupling of the electrophile, plus the amount necessary to reduce the Fe(II) pre-catalyst to Fe(I), indicating that the two homo-coupling processes are intimately linked.

Radical trap investigations

Supplementary Table 18 summarizes the effect of 'radical trap' additives on the coupling of **1a** with **2a**. The addition of 1 equiv. (with respect to **1a**) of either 1,4-cyclohexadiene or 1,1-diphenylethylene had essentially no impact on the extent of either cross- or homo-coupling of the nucleophile, suggesting that free aryl radicals are not formed. Addition of butylated hydroxytoluene (BHT) reduced both the cross- and homo-coupling of the nucleophile, while TEMPO suppressed cross-coupling and increased homo-coupling of the nucleophile, possibly as a result of oxidation of the Fe facilitating subsequent reductive coupling. A similar, but more pronounced effect was observed on

https://doi.org/10.1038/s41929-024-01234-0

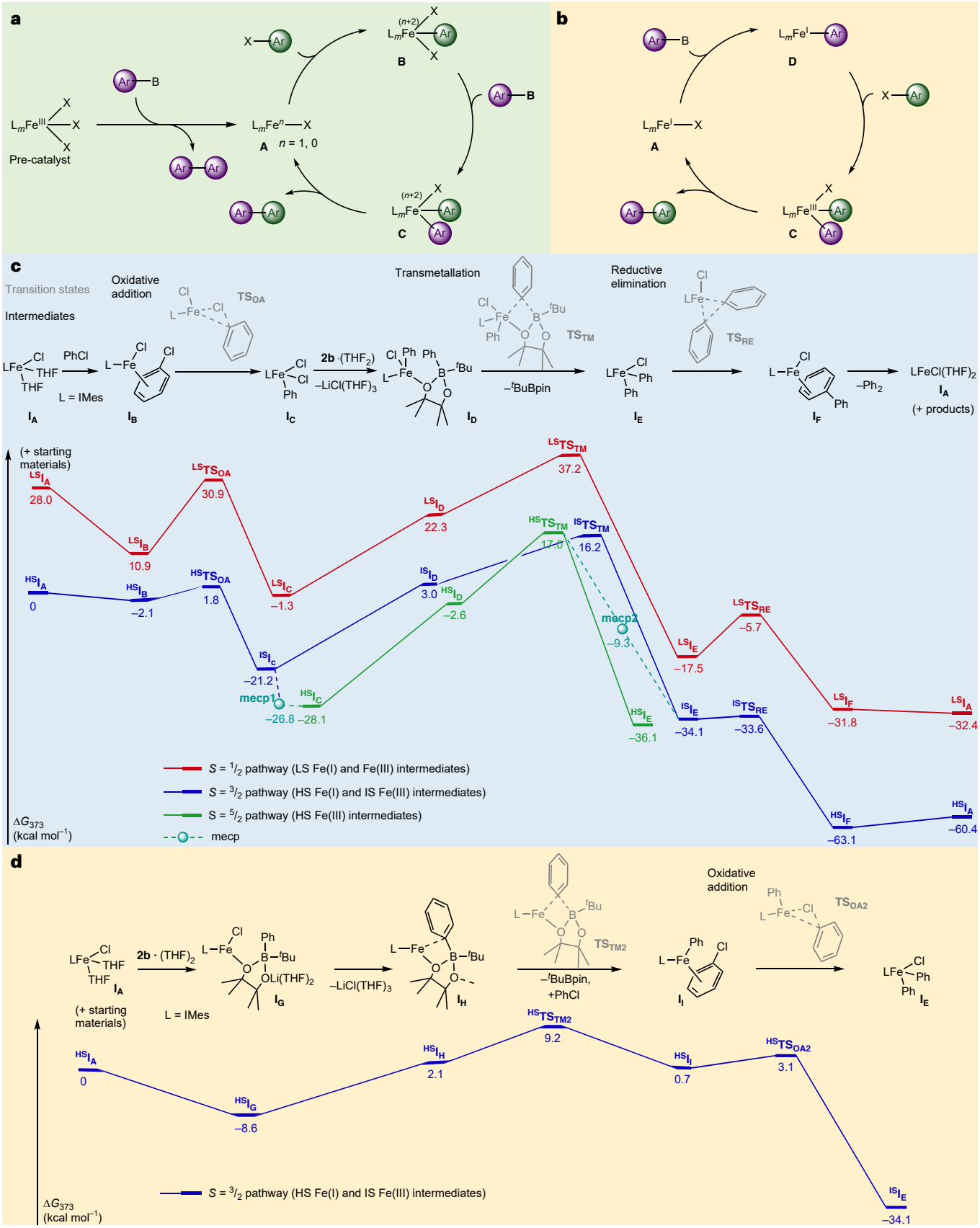

Fig. 7 | Simplified catalytic manifolds and calculated monometallic Fe(I)/(III) pathways. a, Generic structures involved in Fe(I)/Fe(III) or Fe(0)/Fe(II) pathways wherein oxidative addition precedes transmetallation. *n* and *n*+2 refer to arbitrary oxidation states. **b**, An Fe(I)/Fe(III) pathway in which oxidative addition follows transmetallation. **c**, Calculated (PBE0-D3BJ/def2-TZVP(CPCM = THF)//BP86-D3BJ/def2-SVP(def2-TZVP on Fe)) Fe(I)/Fe(III) pathway where oxidative addition precedes transmetallation. **d**, Calculated Fe(I)–Fe(III) pathway with transmetallation preceding oxidative addition. ΔG_{373}, calculated Gibbs free energy at 373K. RE, reductive elimination.

the addition of trityl chloride. Analysing the crude reaction mixtures obtained with BHT, TEMPO and trityl chloride by gas chromatography–mass spectrometry (GC-MS) showed no indication of products formed by reaction of these species with aryl radicals. Taken together, the data show that the formation of aryl radicals from either the aryl chloride or aryl boronate substrates during catalysis can be considered highly unlikely.

Computational investigation of tentative catalytic cycles

Figure 7a,b summarizes the key steps in simplified, monometallic catalytic cycles for the cross-coupling reaction that we have investigated computationally, namely oxidative addition to either Fe(I) or Fe(0) centres followed by transmetallation and reductive elimination, or transmetallation to Fe(I) followed by oxidative addition and then reductive elimination. In addition, we briefly explored the possible involvement of bimetallic intermediates (more below). In all cases, oxidative addition at either mononuclear or binuclear iron centres was modelled favourably as a classical two-electron process (discussion below). While we cannot entirely exclude the possibility that oxidative addition of the aryl chloride occurs via a radical process in one or more of the pathways described, the radical trap evidence above suggests this is unlikely.

The proposed cross-coupling manifolds were probed using density functional theory (DFT) employing the Orca software package[62,63]. Geometries were optimized with the BP86 functional[64] with Grimme's D3 dispersion correction with Becke–Johnson damping[65], employing the def2-TZVP basis set on iron and def2-SVP on all other atoms[66]. Frequency calculations were employed to determine the nature of the stationary states and extract free energies. The Hessians derived from the frequency calculations under standard temperature and pressure were then used to determine the free energies at reaction temperature (373 K). While BP86 gives reliable results for geometry optimizations for first-row metal complexes, the determination of the electronic structure of iron, in particular the energetic separation of the various accessible spin states, can be challenging for DFT, and also highly functional dependent. Therefore, to determine the most appropriate functional for the calculations of interest, we undertook a benchmarking study. The energies of the high, low and (where applicable) intermediate spin states of the representative small model Fe(0)–Fe(III) complexes LFe(PhCl), LFeCl(OMe$_2$), LFeClPh(OMe$_2$) and LFeCl$_2$Ph (L = *N*,*N*′-dimethyl imidazolinylidene) were determined using a local coupled cluster approach, based on BP86-optimized geometries. This was done using the DLPNO-CCSD(T$_1$) approach with improved iterative triple approximations (T$_1$) as implemented in Orca, employing a two-point extrapolation to the PNO space limit[67]. These results were then used to benchmark 14 different DFT functionals (Supplementary Methods for full details). This investigation found that the PBE0 functional[68] with D3BJ dispersion correction gave the lowest variation from the energies determined by the local coupled cluster approach (unsigned variation from average = 5.2 kcal mol^{-1}). The main contribution here for the variation is a poor fit of the energy gap between high-spin (HS, S = 2) and low-spin (LS, S = 0) Fe(II) obtained by the functional and the equivalent energy determined by the local coupled cluster approach (variance = 15.2 kcal mol^{-1}). This was true for most functionals investigated and appears to be an issue with modelling the (highly unlikely for such low-coordinate species) LS Fe(II) spin state. By contrast, the variance between the value calculated using PBE0-D3BJ and dlpno-CCSD(T$_1$) for intermediate spin (IS, S = 1) and HS Fe(II) was less than 1 kcal mol^{-1}.

The final energies of the intermediates modelled in the catalytic cycles were accordingly calculated at the PBE0-D3BJ/def2-TZVP level of theory, with implicit solvation effects accounted for by use of a conductor-like polarizable continuum model (CPCM; full computational details are in the Supplementary Methods). The key findings from this study are summarized in Figs. 7 and 8 and Extended Data Fig. 1, with more information given in the Supplementary Methods.

Figure 7c shows the S = 1/2, S = 3/2 and, where applicable, S = 5/2 pathways for an Fe(I)–Fe(III) manifold in which oxidative addition to Fe(I) occurs prior to transmetallation. It is immediately clear that the S = 1/2 pathway can be disregarded as all intermediates and transition states lie substantially higher in energy than the equivalent species on the next highest energy manifold.

Displacement of the THF ligands of the HS intermediate $^{HS}\mathbf{I_A}$ by PhCl and subsequent oxidative addition is surprisingly facile. Similarly reductive elimination has a very low barrier on the S = 3/2 pathway. Conversely these two redox processes are noticeably more challenging on the doublet pathway. On all three spin surfaces, it is clear that reaction of LFeCl$_2$Ph ($\mathbf{I_C}$) with **2b**·(THF)$_2$ to give the boronate adduct $\mathbf{I_D}$ and LiCl(THF)$_3$ and subsequent transmetallation via transition state $\mathbf{TS_{TM}}$ are the most challenging steps in the calculated cycle. The free energy values of the transition states for the transmetallation on both S = 3/2 and 5/2 pathways are very close (<1 kcal mol^{-1}), with the IS state marginally preferred, while for the Fe(III) intermediates ($\mathbf{I_C}$, $\mathbf{I_D}$ and $\mathbf{I_E}$) the HS state is typically more favourable than the IS state. The calculated spin crossover between $^{IS}\mathbf{I_C}$ and $^{HS}\mathbf{I_C}$ is facile with a readily accessible minimum energy crossing point (**mecp1**) between the two surfaces.

The Fe(III) intermediate $\mathbf{I_E}$ could also be arrived at via an alternative manifold in which transmetallation to Fe(I) precedes the oxidative addition of the aryl chloride, and the S = 3/2 pathway for this transformation starting again from intermediate $^{HS}\mathbf{I_A}$ is shown in Fig. 7d.

We also explored a mononuclear Fe(0)/Fe(II) pathway, and the results are summarized in Fig. 8a and Supplementary Fig. 62. Fig. 8a shows the S = 1 and S = 2 pathways: transition states on the S = 0 pathway could not be identified, but key intermediates modelled on this pathway were far higher in free energy (Supplementary Fig. 62), showing that they could essentially be disregarded. Oxidative addition of PhCl to Fe(0) shows little dependence on explicit solvation, with the transition state for oxidative C–Cl cleavage from $^{HS}\mathbf{I_J}$ (20.4 kcal mol^{-1}, not shown) being very close to the free energy of the oxidative addition transition state $\mathbf{TS_{OA3}}$. Interestingly, it is apparent that oxidative addition to mononuclear (HS) Fe(0) is considerably more challenging than to mononuclear Fe(I). Norrby et al. found a very similar preference for oxidative addition of chlorobenzene to Fe(I) over Fe(0) (ref. 51). Comparing our results with this earlier data indicates that addition of the NHC ligand to Fe(0) has no real impact on the barrier to oxidative addition of PhCl, whereas it lowers the barrier substantially for the Fe(I) intermediates (from ~16 kcal mol^{-1} in the absence of the NHC ligand)[51].

After the oxidative addition to mononuclear Fe(0), the S = 2 path is much preferred to the S = 1 path for the Fe(II) intermediates, and this pathway can be accessed by a minimum energy crossing point (**mecp3**) of −46.8 kcal mol^{-1} close to the structure of intermediate $^{HS}\mathbf{I_L}$. Coordination of the boronate and subsequent transmetallation is challenging for HS Fe(II) ($^{HS}\mathbf{I_L} \rightarrow {}^{HS}\mathbf{I_M} \rightarrow {}^{HS}\mathbf{TS_{TM3}}$ is 32.8 kcal mol^{-1}) but less so than the equivalent steps for HS Fe(III) (45.1 kcal mol^{-1}; details above). Here it seems the coordination of the boronate to the Fe(II) is preferred to coordination to Fe(III), although the $\Delta G^{\ddagger}$ for the transmetallation to Fe(III) (19.6 kcal mol^{-1}) is lower than that for Fe(II) (23.1 kcal mol^{-1}) as might be anticipated for a more electron-deficient metal centre. By contrast, reductive elimination is far more challenging on the Fe(0)/Fe(II) pathway than the Fe(I)/Fe(III) pathways above and requires a spin crossover from the S = 2 to the S = 1 surface. Norrby et al. previously showed that reductive elimination is prohibitively high energy with Fe(II) complexes free of strongly coordinating co-ligands; it appears here that the addition of the NHC ligand partially alleviates this effect[51].

At this stage a consideration of energetic spans (δE)[69] of the various proposed alternatives may prove instructive. For the mono Fe(I) pathway shown in Fig. 7c, the energetic span broadly corresponds with the steps $^{HS}\mathbf{I_C} \rightarrow \rightarrow {}^{HS}\mathbf{TS_{TM}}$ (δE = 45.1 kcal mol^{-1}); for the transmetallation-first pathway (Fig. 7d), the steps are $^{HS}\mathbf{I_G} \rightarrow \rightarrow {}^{HS}\mathbf{TS_{TM2}}$ (δE = 17.8 kcal mol^{-1}), and for the mononuclear Fe(0)/Fe(II) pathway, they are $^{HS}\mathbf{I_L} \rightarrow \rightarrow {}^{HS}\mathbf{TS_{TM3}}$ (δE = 32.8 kcal mol^{-1}). The second of these accords reasonably well

https://doi.org/10.1038/s41929-024-01234-0

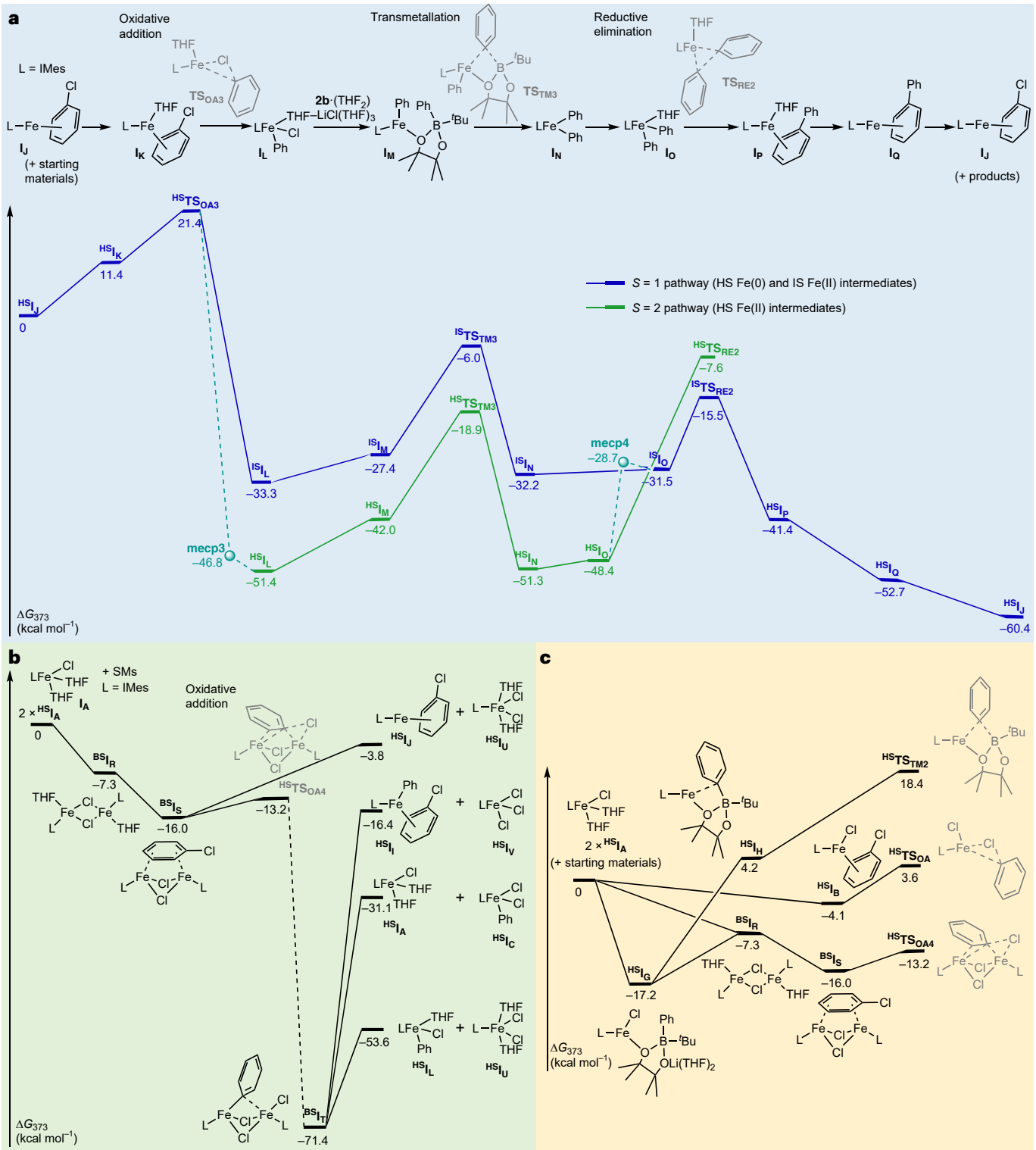

Fig. 8 | Alternative calculated pathways. a, An Fe(0)/Fe(II) pathway. **b**, Dimerisation of Fe(I) followed by either disproportionation or oxidative addition. **c**, Comparing alternative fates of the Fe(I) intermediate $^{HS}\mathbf{I}_A$.

with the experimental value determined above (albeit with the more electron-rich boronate **2a** and in a 2-MeTHF/dioxane solvent mixture) of 22 kcal mol^{-1}, suggesting the Fe(I)/Fe(III), transmetallation-first pathway is more likely to be operative, at least with more electron-rich boronates, than the other two pathways.

Next, we briefly considered the involvement of binuclear iron complexes, and the results from this study are summarized in Fig. 8b. The dimeric intermediates $\mathbf{I}_R$, $\mathbf{I}_S$ and $\mathbf{I}_T$ were first optimized to HS ($S = 3$ for $\mathbf{I}_R$ and $\mathbf{I}_S$; $S = 4$ for $\mathbf{I}_T$) and then to lower-energy broken-symmetry (BS) ground states, with antiferromagnetic coupling observed in each case. The bimetallic oxidative addition transition state $^{HS}\mathbf{TM}_{OA4}$ was determined to be in the $S = 3$ spin state, and a change in spin state from $^{HS}\mathbf{TM}_{OA4} \rightarrow {}^{BS}\mathbf{I}_T$ will clearly be needed, but this has not been investigated further at this stage. It is clear that dimerization of Fe(I) is a thermodynamically favourable process, as is π-coordination of the aryl chloride substrate; as seen with mononuclear Fe(I) species above,

oxidative addition to dimeric Fe(I) is remarkably facile. Post oxidative addition, it is conceivable that the catalysis continues via bimetallic intermediates, but a full investigation of this is beyond the scope of this current study. Alternatively, the resultant Fe(II) dimer may potentially undergo dissociation, and the data in Fig. 8b make clear that this would preferentially produce Fe(II) monomers ($^{HS}\mathbf{I}_L$ and $^{HS}\mathbf{I}_U$) rather than give disproportionation to Fe(I) and Fe(III) species. We also considered the possibility of forming the Fe(II) monomer $^{HS}\mathbf{I}_U$ by disproportionation of the Fe(II) dimer $^{BS}\mathbf{I}_S$, with concomitant formation of one equivalent of the Fe(0) monomer $^{HS}\mathbf{I}_J$, not least as a potential route to a viable Fe(0) catalyst without the need for reduction of the pre-catalyst by the aryl boronate **2**. As can be seen, this is also an energetically accessible pathway.

Figure 8c compares the free energies of various fates that can befall the Fe(I) intermediate $^{HS}\mathbf{I}_A$. Clearly, dimerization, coordination of the boronate or coordination of the aryl chloride are all thermodynamically reasonable, and distinguishing between pathways is challenging. For instance, the reaction of $^{HS}\mathbf{I}_A$ with either boronate **2b** or another equivalent of itself essentially comes down to the probability of collision. This fits well with the observation of a V-shaped Hammett dependency of relative rate with change in boronate electronics: with unsubstituted **2b**, multiple pathways are clearly competitive on the calculated manifolds. The relative population of these manifolds with changing boronate substitution is to be anticipated from the computational results. Furthermore, the computed close-lying energetics of mononuclear and binuclear pathways accords with the observed nonlinear dependence of rate of reaction with varying pre-catalyst concentration.

The production of the Fe(II) intermediate $LFeCl_2(THF)_2$ ($^{HS}I_U$) by (at least) two distinct processes on the dimerization manifold in Fig. 8b provides at least one simple way in which the observed aryl chloride-dependent homo-coupling of **2** might occur, via two sequential transmetallations followed by reductive elimination from the resultant $LFePh_2$ species. The calculated pathway for this process is shown in Extended Data Fig. 1. This makes clear that the first transmetallation to an iron(II) dichloride centre is marginally easier than the second one to an Fe(II)ClPh centre.

Summarizing the calculated catalytic pathways makes it clear that with the unsubstituted aryl boronate **2b**, more than one catalytic manifold is energetically accessible, and indeed competitive under the reaction conditions. This is in accord with both the V-shaped Hammett dependence of relative rates on changing substitution pattern and the nonlinear dependence of rate on pre-catalyst loading. In general, oxidative addition of aryl chlorides to Fe(I) species is far easier than to Fe(0) centres. In all mononuclear pathways examined, the calculated energetic span of the reaction corresponds to the coordination of the boronate to the Fe centre and the subsequent transmetallation, with this becoming more energetically demanding with increasing oxidation state from Fe(I) through to Fe(III). Future investigations will focus on exploring the roles of mononuclear versus polymetallic pathways further from both experimental and computational perspectives.

Conclusions

We have described the iron-catalysed Suzuki biaryl coupling of simple aryl chlorides with aryl boronic esters activated by an organolithium reagent. While issues remain associated with competitive homo-coupling, the results reported here demonstrate that this synthetically challenging—for iron—yet highly desirable transformation is achievable and can accommodate a good range of coupling partners. Furthermore, the results clearly highlight the direction that future studies must take: first, the effective decoupling of the homo- and cross-coupling processes and second, the use of simpler activating agents for the aryl boronic ester substrates. This latter point is particularly important in view of the air and moisture sensitivity of the activated aryl boronates **2**.

Methods

Full experimental details are provided in the Supplementary Methods.

General procedure for in situ preparation of lithium *tert*-butyl aryl boronates

In a Schlenk flask, the appropriate aryl boronic ester (0.62 M, 1.25 or 2.5 mmol) was dissolved in THF or 2-MeTHF (3 or 6 ml). The solution was cooled to −40 °C (acetonitrile/liquid N_2 bath) and *tert*-butyl lithium (1.0 equiv., 1.7 M in pentane) was added dropwise. The solution was stirred for 30 min and then warmed to room temperature and stirred for a further 45 min. This resulting solution was used immediately after preparation. Further details are in the Supplementary Methods.

General procedure for iron-catalysed Suzuki biaryl coupling

In an argon-filled glove box, IMes·HCl (17.1 mg, 0.05 mmol), $FeBr_3$ (14.8 mg, 0.05 mmol), $MgBr_2{\cdot}OEt_2$ (25.8 mg, 0.1 mmol) and the appropriate aryl chloride **1** (0.5 mmol) were added to a dried Schlenk tube containing a stirrer bar, followed by 1,4-dioxane (3.0 ml). In a separate dried Schlenk tube, the appropriate aryl boronate **2** (1.25 mmol) was dissolved in 2-MeTHF (3.0 ml). Both Schlenk tubes were sealed, taken out of the glove box, attached to a Schlenk line and heated to the appropriate temperature (2-MeTHF, 80 °C and 1,4-dioxane, 100 °C) while being stirred. MeMgBr (0.05 ml, 1.0 M, 0.05 mmol) was added to the Schlenk tube containing the pre-catalyst mixture, and the resultant mixture was stirred for 5 min. The aryl boronate-containing solution was then added quickly to the Schlenk tube containing the pre-catalyst mixture, and the resultant mixture was stirred and heated at 100 °C (external temperature) for 3 h. The resulting mixture was cooled to room temperature and quenched with 1.0 M HCl (5.0 ml). The organics were extracted with CH_2Cl_2 (3 × 10 ml); the combined organic layers were dried over $MgSO_4$ and filtered. Some 1,3,5-trimethoxybenzene (internal standard, 84.1 mg, 0.5 mmol) was added, and an aliquot was taken for analysis by ^{1}H NMR spectroscopy. The volatiles were then removed under vacuum. The crude mixture was purified by flash column chromatography (gradient elution, 100% hexanes to 25% ethyl acetate in hexanes) to yield the desired biaryl cross-coupled product **3**.

Data availability

EPR data; NMR data for boron-containing starting materials, cross-coupled products and the mechanistic investigations into the relevance of Fe(0); infrared data for new cross-coupled products; MS data for new cross-coupled products; and *xyz* coordinate files for calculated structures are freely available at https://doi.org/10.5523/bris.1yz60sm9oqq072rutpo77foapu. All other data are available from the authors upon reasonable request.

References

1. Miyaura, N. & Suzuki, A. Palladium-catalyzed cross-coupling reactions of organoboron compounds. *Chem. Rev.* **95**, 2457–2483 (1995).
2. Miyaura, N. *Cross-Coupling Reactions: a Practical Guide* Ch. 2 (Springer, 2002).
3. Suzuki, A. & Yamamoto, Y. Cross-coupling reactions of organoboranes: an easy method for C–C bonding. *Chem. Lett.* **40**, 894–901 (2011).
4. Valente, C. & Organ, M. G. *Boronic Acids* (ed. Hall, D. G.) Ch. 4 (Wiley, 2011).
5. Torborg, C. & Beller, M. Recent applications of palladium-catalyzed coupling reactions in the pharmaceutical, agrochemical, and fine chemical industries. *Adv. Synth. Catal.* **351**, 3027–3043 (2009).
6. Garrett, C. E. & Prasad, K. The art of meeting palladium specifications in active pharmaceutical ingredients produced by Pd-catalyzed reactions. *Adv. Synth. Catal.* **346**, 889–900 (2004).

7. Albrecht, M., Bedford, R. & Plietker, B. Catalytic and organometallic chemistry of earth-abundant metals. *Organometallics* **33**, 5619–5621 (2014).
8. Han, F.-S. Transition-metal-catalyzed Suzuki–Miyaura cross-coupling reactions: a remarkable advance from palladium to nickel catalysts. *Chem. Soc. Rev.* **42**, 5270–5298 (2014).
9. Mastalir, M., Stöger, B., Pittenauer, E., Allmaier, G. & Kirchner, K. Air-stable triazine-based Ni(II) PNP pincer complexes as catalysts for the Suzuki–Miyaura cross-coupling. *Org. Lett.* **18**, 3186–3189 (2016).
10. Zhou, J. et al. NHC nickel-catalyzed Suzuki–Miyaura cross-coupling reactions of aryl boronate esters with perfluorobenzenes. *J. Org. Chem.* **81**, 5789–5794 (2016).
11. Shi, S., Meng, G. & Szostak, M. Synthesis of biaryls through nickel-catalyzed Suzuki–Miyaura coupling of amides by carbon–nitrogen bond cleavage. *Angew. Chem. Int. Ed.* **55**, 6959–6963 (2016).
12. Malan, F. P., Singleton, E., van Rooyen, P. H. & Landman, M. Facile Suzuki-Miyaura coupling of activated aryl halides using new CpNiBr(NHC) complexes. *J. Organomet. Chem.* **813**, 7–14 (2016).
13. Shields, J. D., Gray, E. E. & Doyle, A. G. A modular, air-stable nickel precatalyst. *Org. Lett.* **17**, 2166–2169 (2015).
14. Thapa, S., Shrestha, B., Gurung, S. K. & Giri, R. Copper-catalysed cross-coupling: an untapped potential. *Org. Biomol. Chem.* **13**, 4816–4827 (2015).
15. Gurung, S. K., Thapa, S., Shrestha, B. & Giri, R. Copper-catalysed cross-couplings of arylboronate esters with aryl and heteroaryl iodides and bromides. *Org. Chem. Front.* **2**, 649–653 (2015).
16. Zhou, Y., You, W., Smith, K. B. & Brown, M. K. Copper-catalyzed cross-coupling of boronic esters with aryl iodides and application to the carboboration of alkynes and allenes. *Angew. Chem. Int. Ed.* **53**, 3475–3479 (2014).
17. Gurung, S. K., Thapa, S., Kafle, A., Dickie, D. A. & Giri, R. Copper-catalyzed Suzuki–Miyaura coupling of arylboronate esters: transmetalation with (PN)CuF and identification of intermediates. *Org. Lett.* **16**, 1264–1267 (2014).
18. Neely, J. M., Bezdek, M. J. & Chirik, P. J. Insight into transmetalation enables cobalt-catalyzed Suzuki–Miyaura cross coupling. *ACS Cent. Sci.* **2**, 935–942 (2016).
19. Asghar, S., Tailor, S. B., Elorriaga, D. & Bedford, R. B. Cobalt-catalyzed Suzuki biaryl coupling of aryl halides. *Angew. Chem. Int. Ed.* **56**, 16367–16370 (2017).
20. Duong, H. A., Wu, W. & Teo, Y.-Y. Cobalt-catalyzed cross-coupling reactions of arylboronic esters and aryl halides. *Organometallics* **36**, 4363–4366 (2017).
21. Tailor, S. B. et al. Revisiting claims of the iron-, cobalt-, nickel-, and copper-catalyzed Suzuki biaryl cross-coupling of aryl halides with aryl boronic acids. *Organometallics* **38**, 1770–1777 (2019).
22. Duong, H. A., Yeow, Z.-H., Tiong, Y.-L., Kamal, N. H. B. M. & Wu, W. Cobalt-catalyzed cross-coupling reactions of aryl triflates and lithium arylborates. *J. Org. Chem.* **84**, 12686–12691 (2019).
23. Tailor, S. B., Manzotti, M., Smith, G. J., Davis, S. A. & Bedford, R. B. Cobalt-catalyzed coupling of aryl chlorides with aryl boron esters activated by alkoxides. *ACS Catal.* **11**, 3856–3866 (2021).
24. Bedford, R. B., Hall, M. A., Hodges, G. R., Huwe, M. & Wilkinson, M. C. Simple mixed Fe-Zn catalysts for the Suzuki couplings of tetraarylborates with benzyl halides and 2-halopyridines. *Chem. Commun.* **2009**, 6430–6432 (2009).
25. Hatakeyama, T. et al. Iron-catalyzed Suzuki–Miyaura coupling of alkyl halides. *J. Am. Chem. Soc.* **132**, 10674–10676 (2010).
26. Hashimoto, T., Hatakeyama, T. & Nakamura, M. Stereospecific cross-coupling between alkenylboronates and alkyl halides catalyzed by iron–bisphosphine complexes. *J. Org. Chem.* **77**, 1168–1173 (2012).
27. Hatakeyama, T. et al. Iron-catalyzed alkyl–alkyl Suzuki–Miyaura coupling. *Angew. Chem. Int. Ed.* **51**, 8834–8837 (2012).
28. Bedford, R. B. et al. Expedient iron-catalyzed coupling of alkyl, benzyl and allyl halides with arylboronic esters. *Chem. Eur. J.* **20**, 7935–7938 (2014).
29. Bedford, R. B. et al. Iron phosphine catalyzed cross-coupling of tetraorganoborates and related group 13 nucleophiles with alkyl halides. *Organometallics* **33**, 5767–5780 (2014).
30. Crockett, M. P., Tyrol, C. C., Wong, A. S., Li, B. & Byers, J. A. Iron-catalyzed suzuki–miyaura cross-coupling reactions between alkyl halides and unactivated arylboronic esters. *Org. Lett.* **20**, 5233–5237 (2018).
31. Crockett, M. P., Wong, A. S., Li, B. & Byers, J. A. Rational design of an iron-based catalyst for Suzuki–Miyaura cross- couplings involving heteroaromatic boronic esters and tertiary alkyl electrophiles. *Angew. Chem. Int. Ed.* **59**, 5392–5397 (2020).
32. Bauer, I. & Knölker, H.-J. Iron catalysis in organic synthesis. *Chem. Rev.* **115**, 3170–3387 (2015).
33. Guo, Y., Young, D. J. & Andy Hor, T. S. Palladium-free Suzuki–Miyaura cross-coupling at elevated pressures. *Tetrahedron Lett.* **49**, 5620–5621 (2008).
34. Tailor, S. B. & Bedford, R. B. Can immobilization of an inactive iron species switch on catalytic activity in the suzuki reaction? *Catal. Lett.* **150**, 963–968 (2020).
35. Bedford, R. B., Gallagher, T., Pye, D. R. & Savage, W. Towards iron-catalysed Suzuki biaryl cross-coupling: unusual reactivity of 2-halobenzyl halides. *Synthesis* **47**, 1761–1765 (2015).
36. O'Brien, H. M. et al. Iron-catalysed substrate-directed Suzuki biaryl cross-coupling. *Nat. Catal.* **1**, 429–437 (2018).
37. Ding, K., Zannat, F., Morris, J. C., Brennessel, W. W. & Holland, P. L. Coordination of *N*-methylpyrrolidone to iron(II). *J. Organomet. Chem.* **694**, 4204–4208 (2009).
38. Muñoz, S. B. et al. The *N*-methylpyrrolidone (NMP) effect in iron-catalyzed cross-coupling with simple ferric salts and MeMgBr. *Angew. Chem. Int. Ed.* **57**, 6496–6500 (2018).
39. Nakamura, M., Ito, S., Matsuo, K. & Nakamura, E. Iron-catalyzed chemoselective cross-coupling of primary and secondary alkyl halides with arylzinc reagents. *Synlett* **11**, 1794–1798 (2005).
40. Martin, R. & Fürstner, A. Cross-coupling of alkyl halides with aryl Grignard reagents catalyzed by a low-valent iron complex. *Angew. Chem. Int. Ed.* **43**, 3955–3957 (2004).
41. Bedford, R. B. et al. TMEDA in iron-catalyzed Kumada coupling: amine adduct versus homoleptic 'ate' complex formation. *Angew. Chem. Int. Ed.* **53**, 1804–1808 (2014).
42. Noda, D., Sunada, Y., Hatakeyama, T., Nakamura, M. & Nagashima, H. Effect of TMEDA on iron-catalyzed coupling reactions of ArMgX with alkyl halides. *J. Am. Chem. Soc.* **131**, 6078–6079 (2009).
43. Bedford, R. B. et al. Iron nanoparticles in the coupling of alkyl halides with aryl Grignard reagents. *Chem. Commun.* **2006**, 1398–1400 (2006).
44. Iwamoto, T., Okuzono, C., Adak, L., Jin, M. & Nakamura, M. Iron-catalysed enantioselective Suzuki–Miyaura coupling of racemic alkyl bromides. *Chem. Commun.* **55**, 1128–1131 (2019).
45. Xu, L. et al. The amine-catalysed Suzuki–Miyaura-type coupling of aryl halides and arylboronic acids. *Nat. Catal.* **4**, 71–78 (2021).
46. Novák, Z. et al. Revisiting the amine-catalysed cross-coupling. *Nat. Catal.* **4**, 991–993 (2021).
47. Avanthay, M. et al. Identifying palladium culprits in amine catalysis. *Nat. Catal.* **4**, 994–998 (2021).
48. Vinod, J. K. et al. Fluorometric study on the amine-catalysed Suzuki–Miyaura coupling. *Nat. Catal.* **4**, 999–1001 (2021).
49. Bedford, R. B. How low does iron go? Chasing the active species in Fe-catalyzed cross-coupling reactions. *Acc. Chem. Res.* **48**, 1485–1493 (2015).
50. Zhang, H. et al. (Aminocarbene)(divinyltetramethyldisiloxane) iron(0) compounds: a class of low-coordinate iron(0) reagents. *Angew. Chem. Int. Ed.* **53**, 8432–8436 (2014).

51. Kleimark, J., Hedström, A., Larsson, P.-F., Johansson, C. & Norrby, P.-O. Mechanistic investigation of iron-catalyzed coupling reactions. *ChemCatChem* **1**, 152–161 (2009).
52. Kleimark, J., Larsson, P.-F., Emamy, P., Hedström, A. & Norrby, P.-O. Low temperature studies of iron-catalyzed cross-coupling of alkyl Grignard reagents with aryl electrophiles. *Adv. Synth. Catal.* **354**, 448–456 (2012).
53. Hedström, A., Lindstedt, E. & Norrby, P.-O. On the oxidation state of iron in iron-mediated C–C couplings. *J. Organomet. Chem.* **748**, 51–55 (2013).
54. Bedford, R. B. et al. Iron(I) in Negishi cross-coupling reactions. *J. Am. Chem. Soc.* **14**, 10333–10336 (2012).
55. Bedford, R. B. et al. The highly surprising behaviour of diphosphine ligands in iron-catalysed Negishi cross-coupling. *Nat. Catal.* **2**, 123–133 (2019).
56. Bedford, R. B. et al. Simplifying iron–phosphine catalysts for cross-coupling reactions. *Angew. Chem. Int. Ed.* **52**, 1285–1288 (2013).
57. Burés, J. A simple graphical method to determine the order in catalyst. *Angew. Chem. Int. Ed.* **55**, 2028–2031 (2016).
58. Hansch, C., Leo, A. & Taft, R. W. A survey of Hammett substituent constants and resonance and field parameters. *Chem. Rev.* **91**, 165–195 (1991).
59. Bajo, S., Laidlaw, G., Kennedy, A. R., Sproules, S. & Nelson, D. J. Oxidative addition of aryl electrophiles to a prototypical nickel(0) complex: mechanism and structure/reactivity relationships. *Organometallics* **36**, 1662–1672 (2017).
60. Creary, X. & Mcdonald, S. Methylenecyclopropane rearrangement as a probe for free radical substituent effects. $\sigma^{\bullet}$ values for commonly encountered conjugating and organometallic groups. *J. Org. Chem.* **52**, 3254–3263 (1987).
61. Hedström, A., Izakian, Z., Vreto, I., Wallentin, C.-J. & Norrby, P.-O. On the radical nature of iron-catalyzed cross-coupling reactions. *Chem. Eur. J.* **21**, 5946–5953 (2015).
62. Neese, F. Software update: the ORCA program system, version 4.0. *Wiley Interdiscip. Rev. Comput. Mol. Sci.* **8**, e1327 (2017).
63. Nesse, F. Software update: the ORCA program system—version 5.0. *Wiley Interdiscip. Rev. Comput. Mol. Sci.* **12**, e1606 (2022).
64. Becke, A. D. Density-functional exchange-energy approximation with correct asymptotic behavior. *Phys. Rev. A* **38**, 3098–3100 (1988).
65. Grimme, S., Ehrlich, S. & Goerigk, L. Effect of the damping function in dispersion corrected density functional theory. *J. Comput. Chem.* **32**, 1456–1465 (2011).
66. Weigend, F. & Ahlrichs, R. Balanced basis sets of split valence, triple zeta valence and quadruple zeta valence quality for H to Rn: design and assessment of accuracy. *Phys. Chem. Chem. Phys.* **7**, 3297–3305 (2005).
67. Drosou, M., Mitsopoulou, C. A. & Pantazis, D. A. Reconciling local coupled cluster with multireference approaches for transition metal spin-state energetics. *J. Chem. Theory Comput.* **18**, 3538–3548 (2022).
68. Adamo, C. & Barone, V. Toward reliable density functional methods without adjustable parameters: the PBE0 model. *J. Chem. Phys.* **110**, 6158–6170 (1999).
69. Kozuch, S. & Shaik, S. How to conceptualize catalytic cycles? The energetic span model. *Acc. Chem. Res.* **44**, 101–110 (2011).

Acknowledgements

We thank the laboratory of S. Traxel (Merck Element Analytics) for conducting and evaluating the ICP-MS analyses; the Chemical Synthesis Centre for Doctoral Training (funded by the Engineering and Physical Sciences Research Council (EPSRC; EP/L015366/1), AstraZeneca, GlaxoSmithKline, Syngenta, UCB, Ziylo and the University of Bristol) for the provision of a PhD studentship (B.J.S.R.); the EPSRC for a part studentship and AstraZeneca for CASE top-up funding (H.M.O.); the Technology Enhanced Chemical Synthesis Centre for Doctoral Training, funded by EPSRC (EP/S024107/1), AstraZeneca, Astex, Bayer, GlaxoSmithKline, Syngenta, Vertex and the University of Bristol, for the provision of a PhD studentship (P.R.D.-D.); and the UK Catalysis Hub for resources and support provided via our membership in the UK Catalysis Hub Consortium and funded by EPSRC grant (EP/R026939/1, EP/R026815/1, EP/R026645/1, EP/R027129/1 or EP/M013219/1(biocatalysis)). This work was carried out using the computational facilities of the Advanced Computing Research Centre, University of Bristol (http://www.bristol.ac.uk/acrc/).

Author contributions

B.J.S.R., H.M.O., G.A., P.R.D.-D., J.K., E.R., K.H., I.J.S.F. and R.B.B. designed, performed and analysed the synthetic, catalytic and analytical experiments. R.B.B. designed and performed the computational experiments. R.B.B., B.J.S.R. and G.A. prepared this manuscript.

Competing interests

The authors declare no competing interests.

Additional information

Extended data is available for this paper at https://doi.org/10.1038/s41929-024-01234-0.

Supplementary information The online version contains supplementary material available at https://doi.org/10.1038/s41929-024-01234-0.

Correspondence and requests for materials should be addressed to Robin B. Bedford.

Peer review information *Nature Catalysis* thanks Hans-Joachim Knölker, Per-Ola Norrby and the other, anonymous, reviewer(s) for their contribution to the peer review of this work.

https://doi.org/10.1038/s41929-024-01234-0

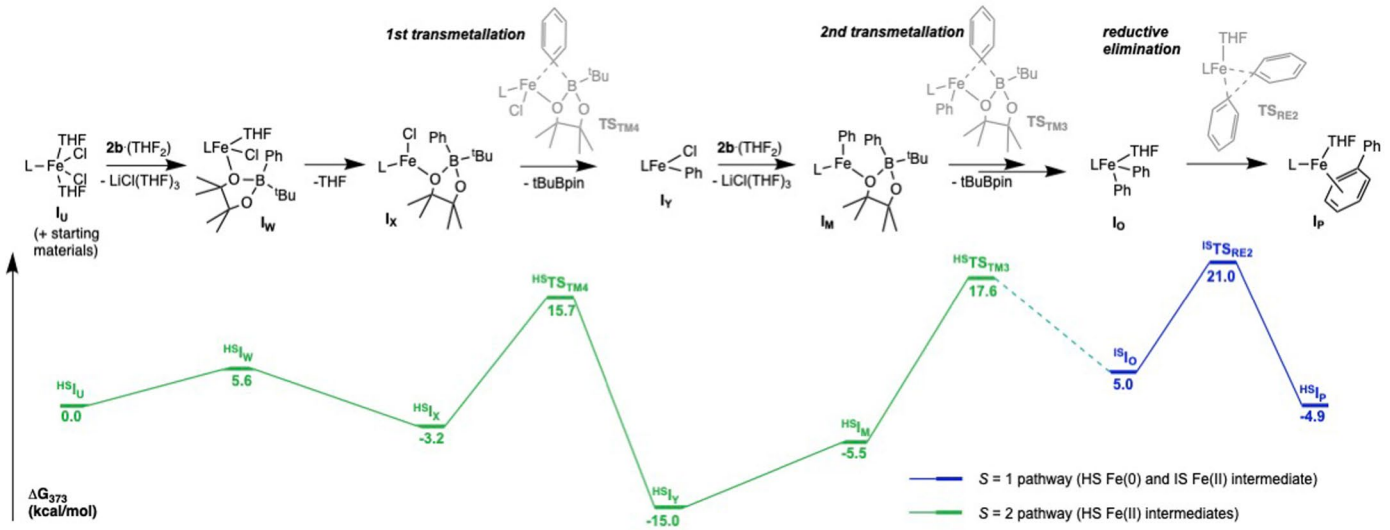

Extended Data Fig. 1 | Representative homocoupling pathway. The free energies of a representative modelled (monometallic) homocoupling reaction involving sequential transmetallation to Fe(II) centres followed by reductive elimination.